

## **Effect of Bulk Acoustic Wave in Piezo Driven Nanomechanical Motion**

**S. K. Roy<sup>1,2,3\*</sup>, W. K. Hiebert<sup>2,3</sup>**

<sup>1</sup>Department of Physics, Chittagong University of Engineering and Technology, Chattogram-4349, Bangladesh

<sup>2</sup>Department of Physics, University of Alberta, Edmonton T6G 2E1, AB, Canada

<sup>3</sup>Nanotechnology Research Centre, National Research Council of Canada, 11421 Saskatchewan Drive, Edmonton T6G 2M9, Canada

Received 4 October 2021, accepted in final revised form 9 November 2021

### **Abstract**

Piezo actuation of mechanical resonators is widely adapted because of its simplicity and versatility. Piezo-driven atomic force microscopy cantilevers in air or liquid have a substantial drawback in that they produce spurious resonances that conceal the cantilever resonance peak. Bulk acoustic wave propagation via the piezo-shaker and device substrate causes these undesired peaks. Such restrictions of piezo actuation are rarely reported in nanomechanical resonant sensing. Because most NEMS (nanoelectromechanical systems) experiments are carried out at low pressure to achieve a higher quality factor ( $Q$ ) and hence increased sensitivity, spurious resonances are frequently overlooked due to their insignificance. However, this piezo-driven issue may affect NEMS responses at higher pressures (lower  $Q$ ) and must be addressed carefully. This study reveals spurious resonances from high vacuum to the atmosphere while investigating piezo-driven nanoscale doubly clamped beam responses. At all pressures, spurious peaks with a characteristic frequency span independent of air damping exist, and at higher pressures, they squeeze the mechanical peak. Such squeezing provides a larger  $Q$  derived from the driven phase responses by order of magnitude than the mechanical  $Q$  computed from the measured thermal noise spectra. Interestingly, the characteristic frequency span, not air damping, is revealed to dominate driven  $Q$ .

*Keywords:* NEMS; Piezo actuation; Quality factor; Spurious resonance; Nanomechanical sensitivity.

© 2022 JSR Publications. ISSN: 2070-0237 (Print); 2070-0245 (Online). All rights reserved.  
doi: <http://dx.doi.org/10.3329/jsr.v14i1.56046>

J. Sci. Res. **14** (1), 269-280 (2022)

## **1. Introduction**

A nanomechanical resonator is a mechanical resonator with one of its dimensions smaller than one micrometer. When a nanomechanical resonator is detected and actuated using electrical methods, it is called a Nanoelectromechanical system (NEMS); however, when it is done using optical methods, it is called a Nano Optomechanical System (NOMS). Over the last few decades, there has been a steady interest in using nanomechanical

---

\* Corresponding author: [skroy@cuet.ac.bd](mailto:skroy@cuet.ac.bd)

devices as ultrasensitive sensors. Because of their small modal mass ( $M_{eff}$ ), they have a high resonance frequency ( $f_0$ ), a high-quality factor ( $Q$ ), and a very small spring constant ( $k_{eff}$ ), and are also responsive to minor perturbations in their surroundings. A small change in the device's mass, temperature, pressure, etc., changes the resonance frequency proportionately. The measurand of interest can thus be quantified by monitoring the accompanying frequency shift. As a result of their physical properties related to mechanical resonance, they have demonstrated a variety of exciting fundamental and applied concepts. They have been extensively studied to detect electron spin dynamics [1], ultra-small forces [2], single-molecule interactions [3,4], and temperature [5]; in addition to single proton mass sensitivity [6], NEMS are extensively studied for quantum information processing [7]. The extraordinary mass sensitivity revealed by NEMS opens the door to developing new generation vacuum mass spectrometers [8]. In contrast to vacuum, the presence of air significantly worsens  $Q$  and signal quality of NEMS [9], resulting in lower frequency resolutions or device sensitivity [10,11], and restricts NEMS applications in ambient conditions. For this reason, most NEMS sensing experiments are found in high vacuum, even at cryogenic conditions [6]. But, mass sensing experiments in biomedical, security screening and environmental monitoring applications require operations at ambient conditions to detect the mass of harmful gaseous or liquid molecules in real-world applications. Our recent article [12] addresses this issue, and our experimental results support our analytical findings that vacuum level nanomechanical sensitivity is attainable at lower  $Q$  experiments. Such unprecedented results have removed the barrier to low- $Q$  NEMS operations, leaving only the difficulty of driving a NEMS at the onset of mechanical nonlinearity at atmospheric pressure. Here, we will discuss the problem's implications and some experimental findings of piezo-driven nanomechanical motion at low- $Q$  conditions that will be relevant for NEMS research and applications.

The smallest detectable measurand that can modify  $f_0$  of NEMS is directly proportional to the device intrinsic frequency stability or Allan deviation,  $\sigma_A$  [10-12]

$$\sigma_A = \frac{\delta f}{f_0} \approx \left( \frac{\Delta f}{Q f_0} \right)^{\frac{1}{2}} \approx \frac{1}{4} \frac{\Delta f}{Q SNR} \quad (1)$$

where, the dynamic range,  $DR = 20 \log \frac{a_c}{a_{th}}$ ,  $a_c \propto Q^{-\frac{1}{2}}$  is the amplitude at the onset of nonlinearity of a nanomechanical resonator,  $a_{th} \propto Q^{\frac{1}{2}}$  is the device's thermal noise peak amplitude,  $\omega_0 = 2\pi f_0$ , and  $f_0$  is the resonance frequency,  $\Delta f$  is the measurement bandwidth. Signal to noise ratio is defined as  $SNR = \frac{a_c}{a_{th}}$ . From equation (1), one can tell that the thermomechanical noise amplitude ( $a_{th}$ ) of the device sets the ultimate limit of frequency resolutions when the device is run at maximum linear  $DR$ , i.e., at the commencement of nonlinearity, which is frequently referred to as critical amplitude ( $a_c$ ). Interestingly, the above relations shows that  $SNR$  improves inversely with damping ( $Q^{-1}$ ) to cancel the damping effect ( $Q$ ) on  $\sigma_A$ . As a result, the reference [12] proves that NEMS sensing in the atmosphere is not a utopia but rather a reality when the device is operated at maximum linear dynamic range. Hence, a suitable readout efficacy of these

tiny NEMS's displacements and suitable actuation techniques is decisive for their technical applications. Recent integrations of nanoscale mechanical resonators to an optical cavity [13] (i.e., a NEMS device) demonstrated exceptional readout competency down to thermomechanical (TM) noise regardless of dampening conditions [12, 13] when compared to their electrical counterpart. Despite substantial progress in nanofabrication and actuation techniques, driving the device at the onset of nonlinearity at low- $Q$  settings (i.e., larger damping scenarios such as atmospheric pressure, liquid operations, and so on) is still a long way off.

There is a range of approaches for actuating NEMS devices, which are adapted from MEMS (Microelectromechanical systems) cantilever actuation systems in atomic force microscopy (AFM), including capacitive, photothermal, magnetic, optical, piezoelectric, and others, each with its own set of advantages and disadvantages [14]. Among these, the popularity of piezoelectric actuation stems from its simplicity and versatility. Inertial actuation with a macroscopic piezo-shaker and direct piezoelectric actuation with an integrated micro- or nanoscale piezoelectric actuator are two types of piezoelectric actuation for nanoscale oscillators. Actuation with a piezo-shaker is often the simplest and most widely utilized actuation technique for lower-frequency devices. However, it frequently results in spurious signals known as "forest of peaks" [15], even at cryogenic operations of NEMS [16], and has been described as bulk acoustic vibration [15-19]. All spurious resonances in the peak forest are not mechanical, which makes them difficult to understand. Identifying the actual NEMS peak from such undesired signal abnormalities [12, 16] and picking an operating frequency for dynamic mode AFM operation of MEMS cantilever in air or liquid also becomes complex [15,17-20]. The response spectrum was a product of the cantilever's broad thermal noise spectrum and an underlying fluid drive spectrum containing the sharp acoustic peaks [15]. Research is currently being conducted to find a solution to this challenge by developing novel actuation techniques by optical means [18] or by introducing an acoustic barrier [19].

Although the AFM community is well aware of these false resonances induced by bulk acoustic waves during piezo-driven mechanical motion, they are rarely understood in NEMS resonant sensing research because most NEMS experiments are carried out in high vacuum to utilize the high  $Q$  effect on sensitivity. In a vacuum, bulk acoustic wave effect on driven NEMS response is negligible due to quasi-static surface amplitude of piezo shaker within a smaller frequency scan [16]. The recent trend of NEMS applications in ambient, e.g. [21], requires more information in low- $Q$  settings where the linewidth of mechanical resonance is too broad. So far, AFM experiments, on the other hand, rarely indicate a bulk acoustic effect on the driven  $Q$ . The goal of this work is to show experimental evidence of bulk acoustic resonances in piezo-driven nanomechanical motion, as well as their impact on the driven quality factor ( $Q_{driven}$ ) at atmospheric pressure. Simultaneously, experimental ways for picking the right driven mechanical peak from such an acoustic "forest of peaks" will be addressed.

## 2. Device and Experiments

The nano-optomechanical system used in the present work and the nanomechanical displacement detection principle are depicted in Figs. 1(a) and (b), respectively. The nanomechanical resonator is a doubly clamped beam (DCB) ( $9.75 \mu\text{m} \times 220 \text{ nm} \times 160 \text{ nm}$ ) and is side coupled to an optical cavity in all-pass configurations. The gap between the DCB NEMS and racetrack optical cavity is  $160 \text{ nm}$ . DCB NEMS motion is detected by the adjacent racetrack optical resonator. In-plane mechanical vibrations of the DCB resonator causes modulations in the gap between the DCB and optical ring resonator and thus modify the local refractive index of the racetrack, which changes the optical resonance wavelength. Consequently, mechanical displacement modulation modulates resonance wavelength ( $\Delta\lambda$  in Fig. 1(b)), which transduces to transmission modulation  $\Delta T$  when probe light is locked at the side slope of the cavity.

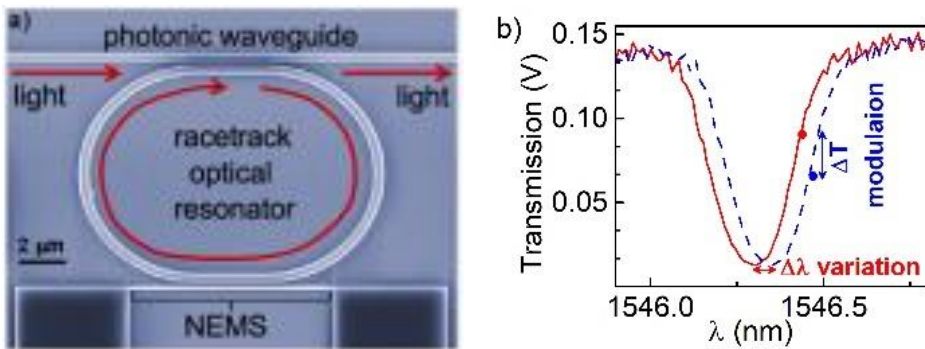


Fig. 1. (a) Scanning electron micrograph of a NOMS made up of a DCB mechanical resonator (bottom), a racetrack optical ring resonator (middle), and a photonic bus waveguide (top). (b) Red plot depicts an experimental cavity resonance spectrum where optical resonance occurs at the dip. Hypothetical blue dashed line epitomizes the concept of optical resonance shift due to adjacent NEMS vibrations. The probe wavelength is set at a steeper slope in the transmission vs. wavelength spectrum so as to transduce NEMS motion into optical power modulation.

Hiebert group at NRC, NRC; Edmonton, AB, Canada developed a confocal nanophotonic measurement system for studying NOMS in a lateral geometry suitable for the foundry-level fabrication of devices. A detail of fabrications and the experimental setup is available in ref. [12,13,23]. The device is housed in a vacuum chamber. The chamber is pumped to a pressure of less than  $100 \mu\text{Torr}$ , and a bleed valve has been used to alter the pressure in the chamber for adjusting the system's damping. Light from a Santec TSL-510 fiber-coupled tunable diode laser (TDL) is coupled from free space via the optical window of the chamber and nanophotonic circuit. With thermal conductive silver epoxy, the NOMS chip is affixed on the piezo-shaker to drive the DCB. Transmission modulations of the optical cavity by mechanical beam motion are read out by a photodiode and measured by a Zurich Instruments HF2 lock-in amplifier (LIA) for

both thermomechanical (TM) and driven signals. The LIA provides the drive voltage to a shear-mode piezo in the wafer plane, which mechanically drives the DCB resonator.

### 3. Results and Discussion

The primary restriction to the precisions of mechanical measurements in the described device system is thermomechanical noise. Thermal noise can be thought of as a driving force that stimulates the mechanical resonance with a constant energy  $k_B T$ , where  $k_B$  denotes the Boltzmann constant, and  $T$  denotes the temperature. A TM noise spectrum of any NEMS represents the ideal resonant response since it carries only mechanical information. So, in order to demonstrate the effect of spurious signals on mechanical resonance, the DCB's TM noise spectra need to be compared to the piezo-driven responses of the same device. For this purpose, the TM noise spectrum at atmospheric pressure (the lowest  $Q$ -setting) is measured and depicted in Fig. 2. Within the recorded 5 MHz spans, the TM noise plot at 760 Torr clearly shows that there is no other peak but the mechanical one.

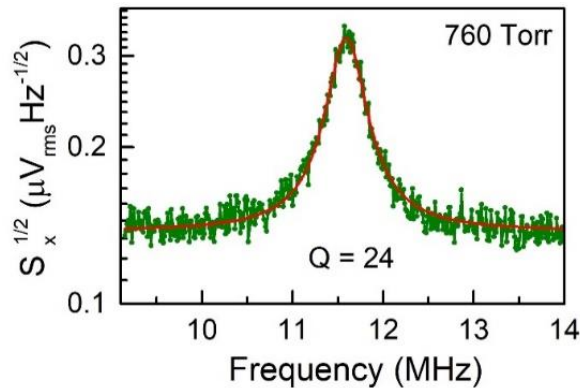


Fig. 2. Measured TM noise spectrum at atmospheric pressure: The spectrum peaks at  $f_0 \sim 11.65$  MHz. It is entirely mechanical because there is no signal from LIA to piezo and is free of any artifacts. The Lorentzian fit at the top of the data is the red line with a linewidth of  $\sim 485,771$  Hz, and the mechanical quality factor,  $Q_{TM} \sim 24$ . Measured voltage signals can be simply translated into displacement in meters using the calibration method described in ref. [12]. All of the signals are expressed in Volt here. Note that peak amplitude of TM noise is,  $a_{th} = \sqrt{S_x(f_0)}$ .

The reverse piezo effect, i.e., deformation of piezoelectric materials in response to an applied electric potential, is used in piezo actuation of mechanical motion. A schematic view of inertial piezo actuation adopted in this work is shown in Fig. 3.

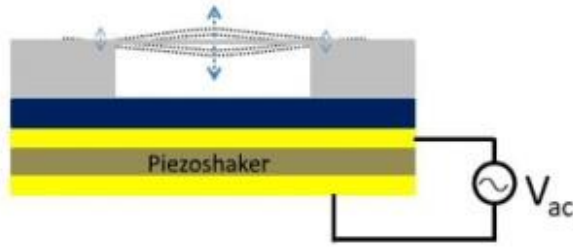


Fig. 3. Schematic illustration of inertial piezo-shaker actuation arrangement in the current work: The motion on the entire chip containing a doubly clamped beam (DCB) is induced by the applied voltage to the piezo. Any periodic inertial force acting on the DCB center of mass drives it into motion in its moving frame of the chip. DCB's resonant amplitude is defined as the range of displacement at its midpoint (long arrow). The effect of the surface acoustic wave is indicated by short arrows on both clamping sides.

The NEMS chip is usually bonded to the piezo-shaker. Mechanical vibration is generated by an excitation voltage applied to the piezo-shaker, which creates stress on the chip surface (see Fig. 3). This stress generates an acoustic wave that travels through the chip to the beam's boundaries and base supports. If most such acoustic waves pass through these barriers and stimulate the DCB vibration, the amplitude and phase curves can have many peaks, resulting in spurious resonances [15-20]. Despite the fact that the acoustic wave effect in piezo-driven mechanical motion is well-known in AFM research, it has received little attention in NEMS research, except the reference [16], which is analogous to AFM cantilever motion.

A damped-driven harmonic oscillator is commonly used to describe the motion of a nanomechanical system. The amplitude of the DCB oscillation in response to a driving frequency applied force is given by the following equation [23]

$$a_{NEMS} = \frac{F_0}{M_{eff} \sqrt{(\omega_0^2 - \omega^2)^2 + (\Gamma\omega)^2}} \quad (2)$$

where,  $F_0$  is the strength of driving force,  $M_{eff}$  is the effective mass of the device,  $\omega_0 = 2\pi f_0$  is the resonance frequency,  $\Gamma = \frac{\omega_0}{Q_{TM}}$  is the damping constant, often known as FWHM (full width half maximum) or linewidth. At resonance, i.e., when  $\omega_0 = \omega$  and  $Q_{TM} \gg 1$ , Eq. (2) reduces to the maximum amplitude as below

$$a_{NEMS} = \frac{F_0 Q_{TM}}{M_{eff} \omega_0^2} \quad (3)$$

where,  $k_{eff} = M_{eff} \omega_0^2$  is the spring constant of the DCB. The piezo-shaker provides the driving force in Eq. (3) in response to the applied voltage, and the displacement is detected by optomechanics described previously. Affixed chip on the piezo-shaker and glue between these makes a complex resonator in which both clamping sides of the DCB can have small constant amplitude,  $a_s$  as in the schematic of Fig. 3. Preferably, a constant frequency independent small oscillation ( $a_s$ ) is expected as at the bottom (dashed line) of

Fig. 4. In such an ideal scenario, the inertial force due to the converse piezoelectric effect acting on the DCB center of mass at its resonance frequency can be written as [16]  $F_0 = M_{eff}\omega_0^2 a_s$ , note that if  $a_s$  becomes frequency-dependent, then the driving force  $F_0$  is also frequency-dependent what is not expected. Hence Eq. (3) gets the following form

$$a_{NEMS} = \frac{M_{eff}\omega_0^2 a_s Q_{TM}}{M_{eff}\omega_0^2} = a_s Q_{TM} \tag{4}$$

which relates the DCB motion at resonance frequency with mechanical  $Q$ , and the amplitude of the substrate motion at clamping points of the resonator. So, if the amplitude ( $a_s$ ) for a high  $Q$  device is frequency independent, i.e., uniform over the frequency sweep range, or is modest and below the instrumental noise floor, the mechanical motion will be unaffected by Eq. (4).

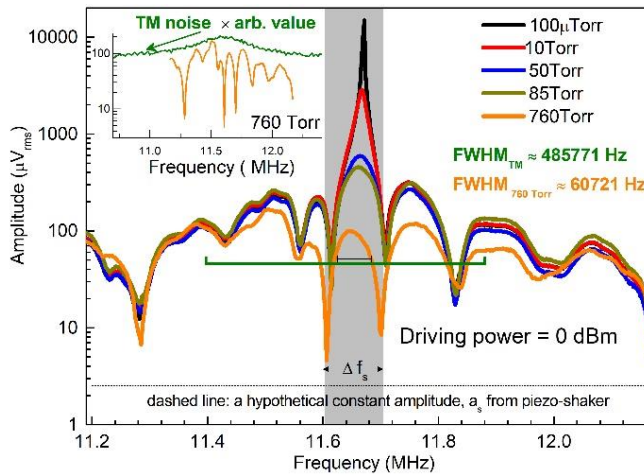


Fig. 4. Piezo-driven amplitude response of the DCB NEMS under 0 dBm constant drive from high vacuum to atmosphere: At 100  $\mu$ Torr, DCB resonance peak appears at  $\sim 11.67$  MHz, i.e., the shaded region represents the characteristic frequency span  $\Delta f_s$  that contains the mechanical motion. A forest of acoustic peaks ( $\Delta f_s$  s) are visible on either side of the resonance peak at all pressures, which are not mechanical because these are pressure independent. Mechanical resonance shift and amplitude drop within the shaded region indicate the air damping effect on the nanomechanical motion [9]. **Inset:** 760 Torr-driven response is plotted with TM noise spectrum of Fig. 2. At 85 and 760 Torr, wider driven mechanical responses ( $\Gamma > \Delta f_s$ ) were clearly compressed by the spatially invariant acoustic peaks on both sides. As a result, 760 Torr FWHM from TM noise is  $8 \times$  higher than that of driven response and provides  $Q_{driven} = 192$  instead of  $Q_{TM} = 24$ .  $Q_{driven} = 192$  fairly agrees with that calculated from phase slope in Fig. 5. Interestingly, 760 Torr TM noise linewidth contains almost  $4 \Delta f_s$ . However, it is verified that except the mechanical one, other  $\Delta f_s$ s are not sensitive.

In experiments, due to bulk acoustic interference, the chip surface moves in a complex spatial and frequency-dependent manner, resulting in frequency-dependent driving strength (i.e.  $a_s$ ), which results in a forest of weak resonances when a broad frequency is spanned. Fig. 4 shows the evolution of the amplitude response of a single NEMS device from a high vacuum to the atmosphere at a constant driving power of 0

dBm. The experimental results in the figure clearly illustrate that during a 1 MHz scan, there are 8 or 9 bulk acoustic peaks, forming a "forest of peaks". It is evident that within each acoustic resonance, there is a characteristic range of driving frequency,  $\Delta f_s$ , where the surface motion may be assumed quasi-uniform. The spatial position and amplitude of each  $\Delta f_s$  remains the same for all pressures. The  $a_s$  within each  $\Delta f_s$  proportionately increases with driving strength  $F_0$  (not shown here). If the magnitude of  $a_s$  is minimum and quasi-uniform inside the  $\Delta f_s$ , a driven high  $Q$  NEMS resonance simply follows Lorentzian Eq. (2), which is free of spurious resonances, similar to TM noise spectra depicted in Fig. 2. Shaded  $\Delta f_s$  contains resonance frequency and thus carries NEMS motion. Outside of this shaded  $\Delta f_s$ , frequency span ( $\Delta f_s$ ) and amplitude ( $a_s$ ) of each spurious resonance are nearly equal at all pressures. As a result, pressure variations have no effect on bulk acoustic resonances, as one might expect. The signal to background ratio of the NEMS resonance peaks is roughly  $60\times$  to  $3\times$  higher than the acoustic background up to about 50 Torr, and the NEMS peaks are easily recognizable. Also,  $Q_{driven} \approx Q_{TM}$  (see Fig. 6). It is evident in Fig. 4 that the NEMS resonance shape is compressed by spatially invariant acoustic resonance when the damping ( $\Gamma$ ) is greater than  $\Delta f$ , as demonstrated in the experimental data at 85 Torr and 760 Torr. Such compression of wider mechanical resonance causes an artificial contraction in the linewidth of driven response which results in a higher effective  $Q$  at larger damping. At the same time, at higher pressures, the amplitude of NEMS and bulk acoustic resonances are similar ( $a_{NEMS} \approx a_s$ ), and certain side peak amplitudes are bigger than the mechanical amplitude, making it difficult to differentiate the real mechanical resonance from such a forest of peaks. Hence, special attention must be taken when identifying the NEMS resonance peaks at highest damping, such as by monitoring the peak from vacuum to atmosphere, in order to correctly determine the appropriate locking frequency range (in this case, within the  $\Delta f_s$  span).

To distinguish the right mechanical peak from the undesirable peak forest at atmospheric pressure, we first measure the high vacuum resonance, then gradually increase the pressure with the vacuum pump's bleed valve, watching the resonance shift as the pressure rises. We may see such resonance shifts on the screen using the HF2 LIA's zi control interface. For example, a screenshot of 760 Torr data plotted in Fig. 4 is shown in the following Fig. 5.

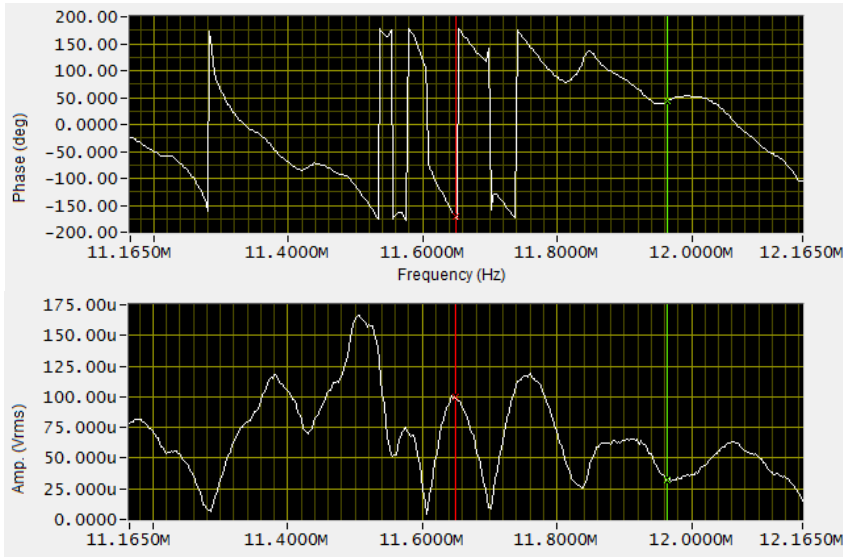


Fig. 5. Screenshot saved by HF2 LIA zi control interface at 760 Torr: 760 torr resonance is found using the HF2 LIA zi control screen by monitoring the resonance at 0 dBm driving power and detecting resonance at each decade of pressure, as shown in Fig. 4. Both amplitude and phase responses can be monitored simultaneously on the screen. The red line on the screen indicates the maximum amplitude of mechanical resonance where the phase slope is the steepest.

A screenshot of the driven amplitude response at 760 Torr (plotted in Fig. 4) is presented along with the corresponding phase response in Fig. 5. It is obvious that each acoustic  $\Delta f_s$ , like the amplitude response, has its phase characteristics and is likewise independent of damping. Damping solely affects the mechanical motion's phase response. Quality factor ( $Q_{driven}$ ) from driven phase response is calculated by

$$Q_{driven} = \frac{f_0}{2} \left| \frac{\partial \varphi}{\partial f} \right|_{f_0} \tag{5}$$

where  $\left| \frac{\partial \varphi}{\partial f} \right|_{f_0}$  is the phase slope at resonance frequency.

From the bottom phase plot of Fig. 5, the calculated phase slope is  $\sim 3.28 \times 10^{-5}$  rad  $\text{Hz}^{-1}$  and yields  $Q_{driven} \sim 191$ , which is in good agreement with the calculated  $Q_{driven}$  from amplitude response in Fig. 4. Similar phase behavior is observed at all other pressures with a change of driven quality factor due to damping. The front panel of zi control also displays calculated  $Q_{driven}$  by itself.

To investigate the effect of air damping on  $Q_{driven}$ , experiments have been performed in a separate chip-piezo combination with the same device presented in Figs. 4 and 5. From high vacuum to atmospheric pressure, TM noise spectra and driven mechanical response at crucial drive power (onset of nonlinearity kicks in at this driving power for corresponding pressure (i.e.,  $Q$ , see Eq. (1)) are measured. The Lorentzian fit of TM noise

spectra and the driven phase response yield  $Q_{TM}$  and  $Q_{driven}$ , respectively. Fig. 6 illustrates the air damping effect on all measured quality factors. The  $Q_{TM}$  vs.  $P$  plot depicts the typical air damping effect.

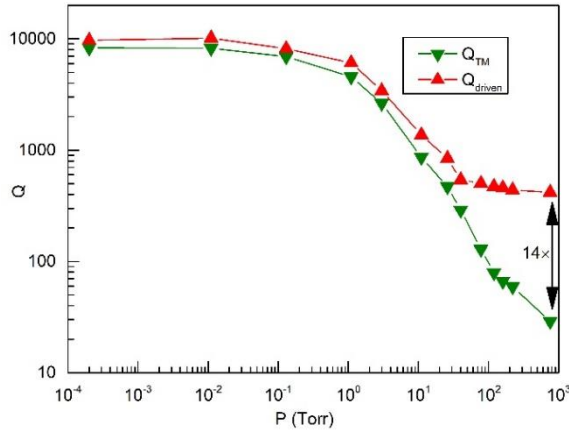


Fig. 6.  $Q_{TM}$  and  $Q_{driven}$  at different pressures:  $Q_{TM}$  vs  $P$  plot represents typical air damping effect on the DCB NEMS and fairly agrees with theory [9, 23]. Experimental results up to  $\sim 40$  Torr shows that  $Q_{TM} \approx Q_{driven}$ . From  $\sim 80$  Torr to 760 Torr (when  $\Gamma > \Delta f_s$ )  $Q_{driven}$  is significantly higher than  $Q_{TM}$ , indicating a bulk acoustic wave effect and  $Q_{driven}$  is independent of air damping. It should be noted that these studies were performed on a different chip from the one shown in Figs. 4 and 5.

The theoretical explanations that underpin the findings are outside the scope of this article and can be found elsewhere [9]. The plot indicates that both measured quality factors are very close, up to about 40 Torr. Because the driven responses are at the critical drive up to 26 Torr, the phase slope may be steeper, resulting in a somewhat higher  $Q_{driven}$ . The 40 Torr amplitude response is too wide to drive at critical amplitude in this study. As a result, driven responses from 40 Torr to 760 Torr are measured at a constant drive level of 36 dBm. In contrast to  $Q_{TM}$ ,  $Q_{driven}$  declines slowly with increasing pressure starting at 40 Torr. According to Fig. 4, such a sluggish change can be attributed to bulk acoustic effect rather than the air damping effect. From 80 Torr, the mechanical linewidth  $\Gamma$  begins to exceed  $\Delta f_s$ , resulting in a substantially higher driven quality factor than the equivalent mechanical one, with  $Q_{driven}$  at 760 Torr being 14 times higher than  $Q_{TM}$ , whereas in Figs. 4 or 5 experiments, it was 8 times. This discrepancy is not surprising. Putman *et al.* [17] investigated the influence of spurious resonance on an AFM cantilever with various sizes of piezo actuators and substrates and discovered a spatial shift and amplitude change in spurious resonance in air and liquid. As a result of the separate silver epoxy bonding of similar DCB chip surface and piezo-shaker, the acoustic wave propagation circumstances may be modified, resulting in a little disparity between determined  $Q_{driven}$  from two sets of experiments described here.

#### 4. Conclusion

Finally, the present study's findings reveal that undesirable spurious resonances can exist at all pressures due to bulk acoustic wave propagation via the piezo-shaker and mounted chip surface on it. An experimental approach for detecting the mechanical peak among these undesired peaks is described when  $\Gamma \gg \Delta f_s$ . This procedure can be employed in NEMS research at both high and low pressures. The magnitude of these bulk acoustic artifacts is solely determined by the driving force applied to the piezo shaker. Air damping does not affect the driving quality factor, which is purely governed by the characteristic frequency span ( $\Delta f_s$ ). In a separate investigation, acoustic artifacts in the driven quality factor were found to not affect device sensitivity or resonant sensing via temperature and gas sensing [21,23]. The mechanical quality factor, calculated by thermal noise spectra, is used in all resonant sensing investigations in reference [21] and [23]. So, all NEMS resonant sensing investigations should use the mechanical quality factor ( $Q_{TM}$ ); otherwise, spurious artifacts in piezo-driven nanomechanical motion might lead to false experimental findings. Future modifications in piezo-actuation or improved approaches are necessary for optimal use of very sensitive NEMS sensors in low- $Q$  operations to get rid of the bulk acoustic effect.

#### Acknowledgments

Nanotechnology Research Centre, National Research Council, Canada supported this research through its fabrication, microscopy, and measurement facilities. CMC Microsystems assisted in fabricating the devices, and postprocessing was done at the University of Alberta nanoFAB.

#### References

1. G. Zolfagharkhani, A. Gaidarzhy, P. Degiovanni, S. Kettemann, P. Fulde, and P. Mohanty, *Nature Nanotechnol.* **3**, 720 (2008). <https://doi.org/10.1038/nnano.2008.311>
2. J. Moser, J. Gutinger, A. Eicher, M. J. Esplandiu, D. E. Liu, M. I. Dykman, and A. Bachtold, *Nature Nanotechnol.* **8**, 493 (2013). <https://doi.org/10.1038/nnano.2013.97>
3. D. Mingdong and O. Sahin. *Nature Communicat.* **2**, 247 (2011). <https://doi.org/10.1038/ncomms1246>
4. A. K. Naik, M. S. Hanay, W. K. Hiebert, X. L. Feng, and M. L. Roukes, *Nature Nanotechnol.* **4**, 445 (2009). <https://doi.org/10.1038/nnano.2009.152>
5. X. C. Zhang, E. B. Myers, J. E. Sader, and M. L. Roukes, *Nano lett.* **13**, 1528 (2013). <https://doi.org/10.1021/nl304687p>
6. J. Chaste, A. Eichler, J. Moser, G. Ceballos, R. Rurali, and A. Bachtold, *Nature Nanotechnol.* **7**, 301 (2012). <https://doi.org/10.1038/nnano.2012.42>
7. D. Kielpinski, C. Monroe, and D. J. Wineland, *Nature* **417**, 709 (2002). <https://doi.org/10.1038/nature00784>
8. E. Sage, M. Sansa, S. Fostner, M. Defoort, M. Gély, A. K. Naik, R. Morel, L. Duraffourg, M. L. Roukes, T. Alava, and G. Jourdan, *Nature Communicat.* **9**, 1 (2018). <https://doi.org/10.1038/s41467-018-05783-4>
9. O. Svitelskiy, V. Sauer, N. Liu, K. M. Cheng, E. Finley, M. R. Freeman, and W. K. Hiebert, *Phys. Rev. Lett.* **103**, ID 244501 (2009). <https://doi.org/10.1103/PhysRevLett.103.244501>

10. K. L. Ekinci, Y. T. Yang, and M. L. Roukes, *J. Appl. Phys.* **95**, 2682 (2004).  
<https://doi.org/10.1063/1.1642738>
11. M. Sansa, E. Sage, E. C. Bullard, M. Gély, T. Alava, E. Colinet, A. K. Naik, L. G. Villanueva, L. Duraffourg, M. L. Roukes, and G. Jourdan, *Nature Nanotechnol.* **11**, 552 (2016).  
<https://doi.org/10.1038/nnano.2016.19>
12. S. K. Roy, V. T. Sauer, J. N. Westwood-Bachman, A. Venkatasubramanian, and W. K. Hiebert, *Science* **360** (2018). <https://doi.org/10.1126/science.aar5220>
13. V. T. K. Sauer, Z. Diao, M. R. Freeman, and W. K. Hiebert. *Nanotechnol.* **25**, ID 055202 (2014). <https://doi.org/10.1088/0957-4484/25/5/055202>
14. T. Kouch, M. S. Hanay, and K. L. Ekinci. *Micromachines* **8**,108 (2017).  
<https://doi.org/10.3390/mi8040108>
15. T. E. Schäffer, J. P. Cleveland, F. Ohnesorge, D. A. Walters, and P. K. Hansma, *J. Appl. Phys.* **80**, 3622 (1996). <https://doi.org/10.1063/1.363308>
16. I. Bargatin, PhD Thesis, California Institute of Technology, USA (2008).
17. C. A. Putman, K.O. Van der Werf, B. G. De Grooth, N. F. Van Hulst, and J. Greve, *Appl. Phys. Lett.* **64**, 2454 (1994). <https://doi.org/10.1063/1.111597>
18. Y. Miyahara, H. Griffin, A. Roy-Gobeil, R. Belyansky, H. Bergeron, J. Bustamante, and P. Grutter, *EPJ Techniques Instrumentation* **7**, 2 (2020).  
<https://doi.org/10.1140/epjti/s40485-020-0053-9>
19. H. Asakawa and T. Fukuma, *Rev. Scientific Instruments* **80**, 103703 (2009).  
<https://doi.org/10.1063/1.3238484>
20. C. Carrasco, P. Ares, P. J. De Pablo, and J. Gómez-Herrero, *Rev. Scientific Instruments* **79**, 126106 (2008). <https://doi.org/10.1063/1.3053369>
21. A. Venkatasubramanian, V. T. Sauer, S. K. Roy, M. Xia, D. S. Wishart, and W. K. Hiebert, *Nano Lett.* **16**, 6975 (2016). <https://doi.org/10.1021/acs.nanolett.6b03066>
22. Z. Diao, J. E. Losby, V. T. K. Sauer, J. N. Westwood, M. R. Freeman, and W. K. Hiebert, *Appl. Phys. Express* **6**, ID 065202 (2013). <https://doi.org/10.7567/APEX.6.065202>
23. S. K. Roy, PhD Thesis, University of Alberta, Canada (2019). <https://doi.org/10.7939/r3-4ayq-bn15b>